

1 **Technical Note: Monitoring discharge of mountain streams by**
2 **retrieving image features with deep learning**

3 Chenqi Fang¹, Genyu Yuan¹, Ziyang Zheng¹, Qirui Zhong¹, Kai Duan^{1*}

4 ¹ *School of Civil Engineering, Sun Yat-Sen University, Guangzhou, China*

5 *Corresponding author, E-mail: duank6@mail.sysu.edu.cn

6 **Abstract**

7 Traditional discharge monitoring usually relies on measuring flow velocity and cross-
8 section area with various velocimeters or remote-sensing approaches. However, the
9 topography of mountain streams in remote sites largely hinders the applicability of
10 velocity-area methods. We here present a method to continuously monitor mountain
11 stream discharge using a low-cost commercial camera and deep learning algorithm. A
12 procedure of automated image categorization and discharge classification was
13 developed to extract information on flow patterns and volumes from high-frequency
14 red–green–blue (RGB) images with deep convolutional neural networks (CNNs). The
15 method was tested at a small, steep, natural stream reach in southern China. Reference
16 discharge data was acquired from a V-shaped weir and ultrasonic flowmeter installed a
17 few meters downstream of the camera system. Results show that the discharge-relevant
18 stream features implicitly embedded in RGB information can be effectively recognized
19 and retrieved by CNN to achieve satisfactory performance in discharge measurement.
20 Coupling CNN and traditional machine learning models (e.g., support vector machine
21 and random forest) can potentially synthesize individual models’ diverse merits and
22 improve generalization performance. Besides, proper image pre-processing and
23 categorization are critical for enhancing the robustness and applicability of the method
24 under environmental disturbances (e.g., weather and vegetation on river banks). Our
25 study highlights the usefulness of deep learning in analyzing complex flow images and
26 tracking flow changes over time, which provides a reliable and flexible alternative

27 apparatus for continuous discharge monitoring of rocky mountain streams.

28 **Keywords:**

29 Discharge monitoring; Mountain streams; Deep learning; Machine learning; Image
30 categorization

31 **1 Introduction**

32 Continuous discharge data is critical for hydrological model development and flood
33 forecast (Clarke, 1999; Mcmillan et al., 2010), water resources management (Council,
34 2004), and aquatic ecosystem health assessment (Carlisle et al., 2017). Traditional
35 discharge monitoring relies on stream gauges that convert water level to discharge with
36 an established stage-discharge curve, or information on stable cross-sections and flow
37 velocity obtained from flow velocimeters such as acoustic doppler current profiler
38 (ADCP) and ultrasonic defectoscope (Kasuga et al., 2003). However, these approaches
39 require significant investment on the implementation of equipments, training of
40 personnel with expertise, and constant maintenance (Fujita et al., 2007; Czuba et al.,
41 2017; Yorke and Oberg, 2002). Besides, the performance of transducers and
42 velocimeters is usually susceptible to sediments and floating debris, particularly in
43 flooding seasons (Hannah et al., 2011). Consequently, large temporal gaps remain in
44 many discharge records across the world despite of the growing demand on data
45 (Davids et al., 2019; Royem et al., 2012). Spatially, flow monitoring of downstream
46 river sections has been assigned to a higher priority due to the concerns on water supply
47 and flood control, leading to an acute shortage of discharge data in mountain streams

48 and headwater catchments (Deweber et al., 2014).

49 To overcome the limitations of traditional methods, a few image-based approaches
50 have been introduced into water stage, flow velocity, and discharge measurement in
51 rivers (Noto et al., 2022; Leduc et al., 2018). Image-based (Leduc et al., 2018; Noto et
52 al., 2022) approaches rely only on the acquisition of digital images of streams from
53 inexpensive commercial cameras and thus have been a promising alternative for
54 continuous, noninvasive, and low-cost streamflow monitoring. The two most
55 commonly used approaches include large-scale particle image velocimetry (LSPIV)
56 and particle tracking velocimetry (PTV). LSPIV (Fujita et al., 2010) is based on a high-
57 speed cross-correlation scheme between an interrogation area (IA) in a first image and
58 IAs within a search region (SR) in a second image. The technique has been proved
59 effective in monitoring low-velocity and shallow-depth flow fields (Tauro et al., 2018).
60 However, it performs poorly in mapping velocity fields in high resolution when there
61 is a lacking of seeds on the water surface because the algorithm obtains the average
62 speed of each SR (Tauro et al., 2017). Compared to LSPIV, PTV was designed for low
63 seeding density flows, focusing on particle tracking instead of recognition. The PTV
64 approach does not require assumptions on flow steadiness nor the relative position of
65 neighbor particles (Tauro et al., 2018). Several algorithms have been developed for PTV
66 analysis, such as space-time image velocimetry (STIV) and optical tracking
67 velocimetry (OTV), overcoming the over-dependence on natural particles' shape and
68 size (Tauro et al., 2018; Tsubaki, 2017). STIV evaluates surface flow velocity by

69 analyzing a texture angle within a variation of brightness or color on the water surface,
70 while OTV combines automatic feature detection, Lucas-Kanade tracking algorithm
71 and track-based filtering methods to estimate subpixel displacements (Fujita et al., 2007;
72 Karvonen, 2016). Existing image-based discharge measurement methods all use the
73 velocity-area method to indirectly deduce discharge after identifying stage and average
74 (Davids et al., 2019; Leduc et al., 2018; Tsubaki, 2017; Herzog et al., 2022) velocity.
75 The average velocity in a cross-section is estimated with surface velocity derived from
76 natural or artificial seeds on water surface and pre-defined empirical relationships
77 between the surface velocity and average velocity. The velocity-area method relies on
78 a stable relationship between stage and cross-sectional area, and needs to take velocity
79 extrapolations to the edges and vertical distributions throughout the cross-section into
80 account (Le Coz et al., 2012). However, it is difficult to identify the water stage and
81 vertical characteristics of mountain streams due to the steep, narrow, and highly
82 heterogeneous cross-sections. The applicability of PIV and PTV approaches is largely
83 hindered by such topography.

84 Unlike PIV and PTV, deep learning models possess the capability to extract
85 discharge-related features from images of rivers or streams automatically. These models
86 are able to adjust the weights assigned to each feature, eliminating the need for manual
87 attention and reducing the risk of overemphasizing or misinterpreting features that are
88 unresponsive to flow discharge (Canziani et al., 2016). Besides, deep learning models
89 can extract low-level image features, such as edges, textures, and colors (Jiang et al.,

90 2021). These merits could be essential in retrieving information from images of
91 mountain streams, particularly in regions with intricate cross-sectional profiles.

92 In this study, we propose a novel mountain stream discharge monitoring method
93 using a low-cost commercial camera and deep learning models. Automated image
94 categorization and pre-processing procedures were developed for processing high-
95 frequency red–green–blue (RGB) images, and then the convolutional neural network
96 (CNN) was used to extract information on flow patterns from RGB matrixes and
97 establish empirical relationships with the classification probabilities of discharge
98 volumes. We hypothesize that (1) the features of mountain streams (e.g., coverage of
99 water surface, flow direction, flow velocity) embedded in RGB images can be
100 recognized by suitable deep learning approaches to achieve effective discharge
101 monitoring, and (2) proper image pre-processing and categorization can improve
102 accuracy of image-based discharge monitoring of mountain streams. A rocky mountain
103 stream of a headwater catchment in tropical southern China was used as a study site to
104 test our hypotheses.

105

106 **2 Methods**

107 **2.1 Site and field setting**

108 The study site is located on a small, steep, rocky reach of a stream in the Zhuhai Campus
109 of Sun Yat-sen University, China (22°20'58" N, 113°34'29" E). The site elevation is 13
110 m above sea level and about 2 km away from the Lingding Yang of South China Sea.

111 The stream flow is mainly controlled by rainfall in the upstream drainage area. Water
112 stage and flow velocity increase rapidly during East Asian summer monsoon rainfalls
113 and fluctuate with synoptic weather conditions on dry days.

114 The main objective of the study was to test the applicability of deep-learning based
115 image processing approaches in capturing the flow characteristics and discharge
116 volumes in the daily flow cycle in this mountain stream. We selected a straight, single-
117 thread reach for the gauging location, and set up a Hikvision camera on the left bank of
118 the stream to collect flow images (**Fig. 1**). Discharge data monitored by a weir about 8
119 m downstream of the camera was used for model training and validation. The camera
120 was installed 3 m above the ground, facing the surface of the stream almost vertically.
121 The entire stream width is visible in the images. The camera was equipped with a 150W
122 solar panel and 80AH lithium battery, enabling the camera to work continuously for 80
123 hours without external power on rainy days. The camera supports the wireless
124 transmission of video data to the server.

125



126

127 **Figure 1.** Camera setup. The camera is set on the left bank of the stream, about 3 m
 128 above the water surface, and 8 m upstream of a gauging weir.

129

130 2.2 Data

131 The flat V-shaped weir downstream of the camera monitors discharge with an open
 132 channel flowmeter and an overflow flowmeter. The flowmeters measure water levels in
 133 the channel and in front of the weir with ultrasonic sensors and calculate real-time
 134 discharge at the time step of two minutes by a semi-empirical equation suggested by
 135 the State Bureau of Technical Supervision of China (www.chinesestandard.net), as

$$136 \quad Q = \frac{8}{15} C_e \tan \frac{\theta}{2} \sqrt{2gh_e^{\frac{5}{2}}} \quad (1)$$

137 where Q is the discharge of stream, θ is the angle of triangular weir, g is

138 acceleration of gravity, h_e is the height of the water surface from the bottom of triangle
139 barrier, C_e is an empirical coefficient.

140 We collected the discharge data of the weir and its corresponding stream videos
141 during daylight (07:00-19:00 UTC+8) from July 20th to September 27th, 2022. The raw
142 video resolution was 2560×1440 pixels with a refresh rate of 50 Hz. Images were
143 extracted from the videos at 5-minute intervals to avoid excessive similarity between
144 adjacent images. A total of 7,757 image samples labeled with 37 discharge values
145 between 0.014 and 0.050 m³/s at the interval of 0.001 m³/s were collected for model
146 testing.

147 **2.3 Image processing**

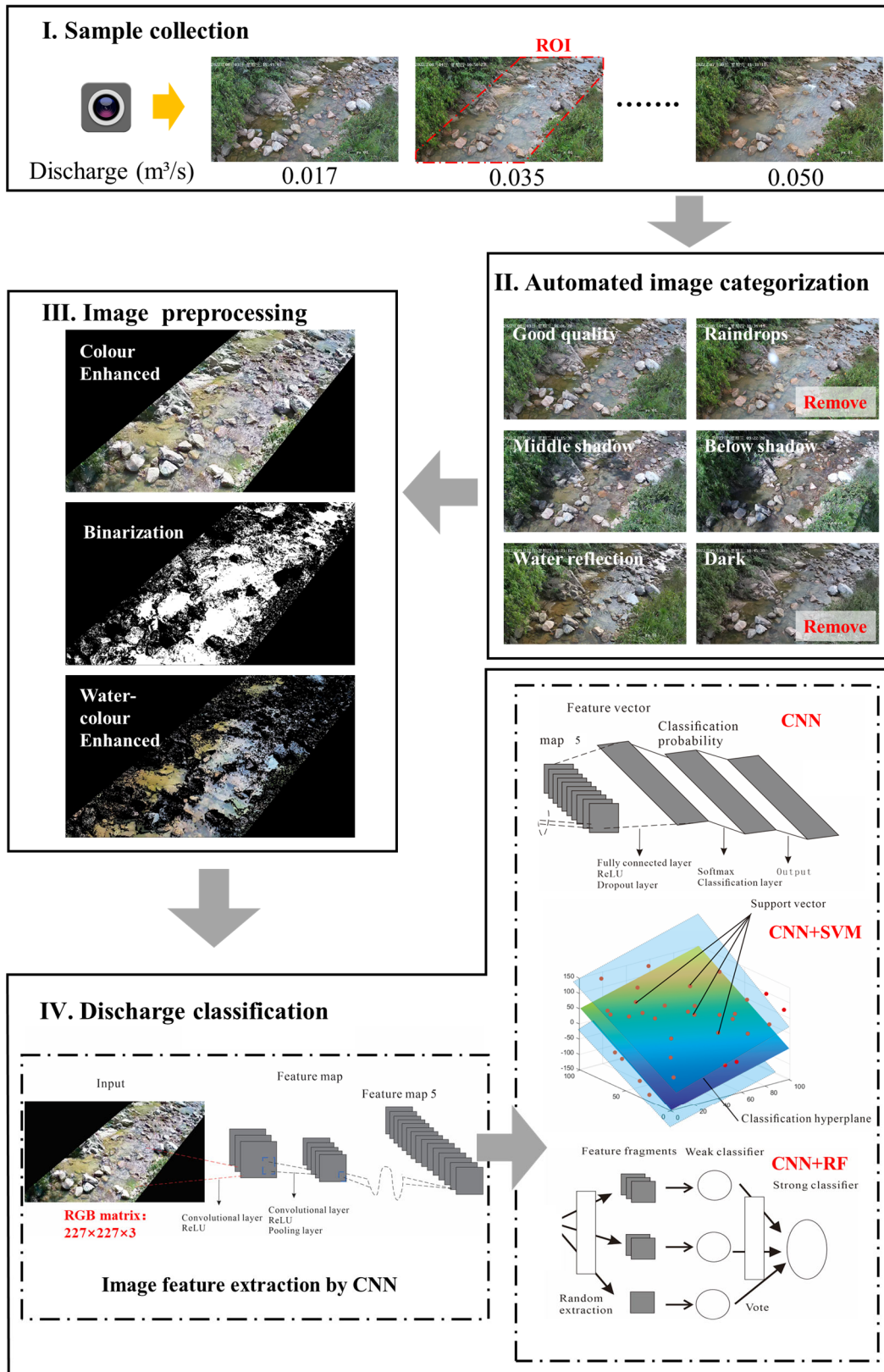
148 **2.3.1 Image categorization**

149 Environmental disturbances such as illumination and shadow can seriously interfere
150 with the extraction of effective image features of mountain streams, such as boundaries
151 of water surface and textures of flow lines (Herzog et al., 2022; Gershon et al., 1986).
152 Although researchers have proposed methods to eliminate shadows (Finlayson et al.,
153 2002), the treatment effect in some complex environments, such as plant shadows and
154 boulders distributed on mountain streams, is not always satisfactory.

155 Frequently observed disturbances on images include: (1) shadows in the target stream
156 region due to plants blocking direct sunlight; (2) image noise due to raindrops attached
157 to the camera lens on rainy days; (3) the lack of light leading to low brightness and
158 contrast of the image; (4) overexposure of image due to light reflection of the water

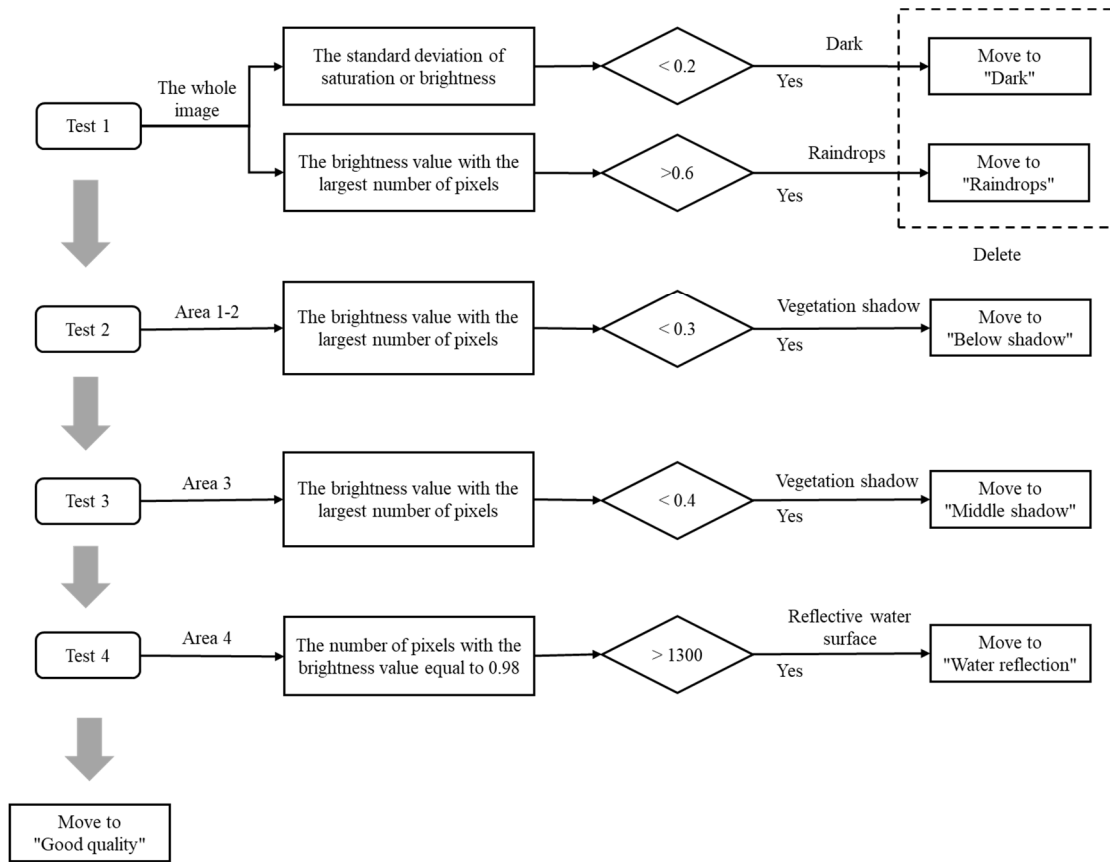
159 surface (around 16:00 UTC+8 in this case). Taking these factors into consideration, we
160 divided all image samples into six categories, including "Good quality", "Raindrops",
161 "Middle shadow", "Below shadow", "Water reflection", and "Dark" (**Fig. 2**). "Good
162 quality" contains image samples without obvious noise or shadow. All the other images
163 lose some feature information due to noise, shadows, reflections, or dim lighting. To
164 ensure the model performance under different environmental conditions, we designed
165 an automated categorization procedure (**Fig. 3**) to screen the raw images and exclude
166 the "Raindrops" and "Dark" samples from model training.

167



168

169 **Figure 2.** Flowchart of image processing and discharge monitoring.



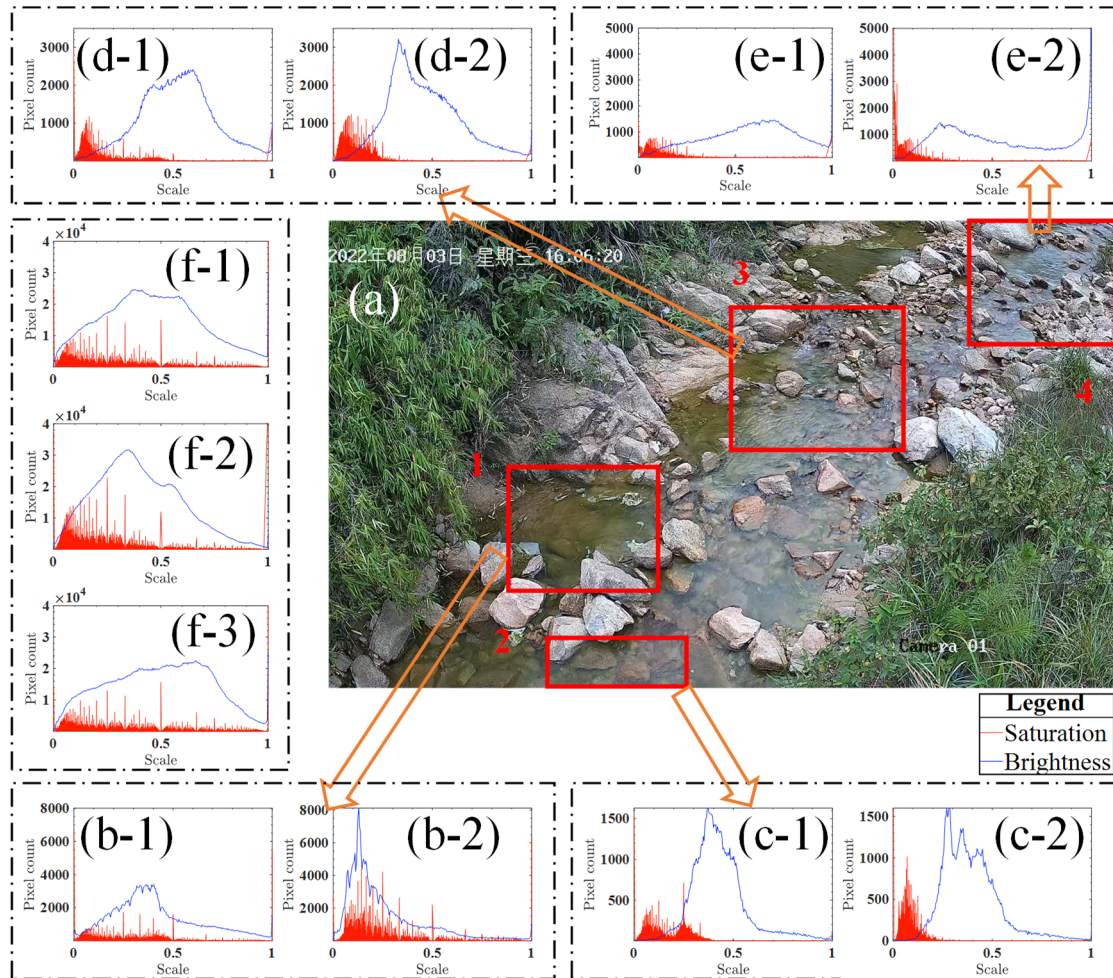
171

172 **Figure 3. Procedure of automated image categorization.**

173

174 Firstly, we selected four areas in the image as the detection areas (**Fig. 4a**) where the
 175 special conditions mentioned above commonly occurred: the upper and lower shadows
 176 in the target stream section mainly appeared in Area 3 and Area 1&2, respectively;
 177 disturbance of water surface reflection was mostly found in Area 4. Then, the thresholds
 178 of saturation or brightness in the four detection areas for image categorization were
 179 determined manually by comparing image samples under different conditions. The
 180 four-step procedure includes: (1) "Dark" images (**Fig. 4f-2**) were identified when the
 181 standard deviation of the brightness or saturation of the full image was less than 0.2. (2)

182 "Raindrops" images (**Fig. 4f-3**) were identified when the brightness of the whole image
183 with the largest number of pixels was greater than 0.6. These two types of images were
184 excluded from the training samples. (3) "Below shadow" (**Fig. 4b-2; Fig. 4c-2**) and
185 "Middle shadow" images (**Fig. 4d-2**) were identified when the brightness value with
186 the largest number of pixels in Area 1&2 and Area 3 was less than 0.3 and 0.4,
187 respectively. (4) "Water reflection" images were identified when the number of pixels
188 with a brightness value of 0.98 in Area 4 exceeded 1300 (**Fig. 4e-2**). The images passing
189 all the tests in the procedure were considered "Good quality" samples. The other charts
190 in **Fig. 4** show the saturation and brightness distributions derived from a typical "Good
191 quality" image.



192

193 **Figure 4.** Comparison of saturation and brightness distributions in the four detection
 194 areas under different environmental conditions. The horizontal axis is the interval range
 195 (0-1) of saturation and brightness in HSB space. The vertical axis indicates the number
 196 of pixels under a certain saturation or brightness value. **Figures b-1, c-1, d-1, and e-1**
 197 **display the saturation and brightness distributions in Area 1-4 of a “Good quality”**
 198 **sample. Figures b-2, c-2, d-2, and e-2 display the results derived from samples of**
 199 **“Below shadow” (b-2; c-2), “Middle shadow” (d-2), and “Water reflection” (e-2),**
 200 **respectively. Figures f-1, f-2, and f-3 display the saturation and brightness distributions**
 201 **of an entire image, derived from “Good quality”, “Dark”, and “Raindrops” samples,**

202 respectively.

203

204 2.3.2 Color enhancement

205 In order to highlight the stream features embedded in the images and avoid image
206 information redundancy, we compared three commonly used color enhancement
207 approaches to process the image samples.

208 **(1) Color Enhanced.** A dynamic histogram equalization technique (Abdullah-Al-
209 Wadud et al., 2007; Cheng and Shi, 2004) was used to enhance contrast and emphasize
210 stream features. First, vegetation areas on both sides of the stream were cropped and
211 filled with black. Then, histogram equalization was used to enhance the contrast
212 between light and dark, i.e., brighten the bubbles, swirls, ripples, splashes, water
213 coverage, etc., and darken the bottom stones and reflections in the water.

214 **(2) Binarization.** Binarization of image information can decrease the
215 computational load and enable the utilization of simplified methods compared to 256
216 levels of grey-scale or RGB color information (Finlayson et al., 2002; Sauvola and
217 Pietikäinen, 2000). In this case, the RGB and HSB (Hue, Saturation, Brightness)
218 information extracted from images suggests that the brightness of the stream water
219 under daylight ranges from 0.2 to 0.7, and the values of three color components follow:

$$220 \quad R(x, y) + G(x, y) + B(x, y) > 350 \quad (2)$$

221 Where $R(x, y)$, $G(x, y)$ and $B(x, y)$ respectively represent the red, green, and blue
222 color values of the pixel (x, y) . The original image was transformed into a binary image

223 by assigning the values of "1" and "0" to the pixels within and out of the water body,
224 respectively.

225 **(3) Water-color Enhanced.** Considering that water-color features may carry some
226 useful information on discharge (Kim et al., 2019), we tested a new pre-processing
227 method combining the two approaches above. The RGB information of the original
228 image within the water body areas was kept unchanged, while the non-water body areas
229 were filled with black color. Then, the water body areas were further enhanced with the
230 histogram equalization method to highlight the edge transition between the water body
231 and the background (Abdullah-Al-Wadud et al., 2007).

232 2.3.3 Image denoising

233 Images pre-processed by all of three approaches still contain large amounts of noise
234 due to environmental disturbances and edge oversharpening caused by image contrast
235 enhancement (Herzog et al., 2022). Therefore, the wavelet transform (Zhang, 2019) was
236 adopted to denoise the image samples. We chose a compromise threshold between hard
237 and soft thresholds as the threshold function (Chang et al., 2010). When the wavelet
238 coefficient is greater than or equal to the threshold, a compromise coefficient α ranging
239 from 0 to 1 is added before the threshold to achieve a smooth transition from hard to
240 soft thresholds, as

$$241 \quad \lambda = \frac{\text{median}(d_j(k))}{0.6745} \times \sqrt{2 \log(M \times N)} \quad (3)$$

$$242 \quad \omega_\lambda = \begin{cases} [\text{sign}(\omega)](|\omega| - \alpha\lambda), & |\omega| \geq \lambda \\ 0, & |\omega| < \lambda \end{cases} \quad (4)$$

243 where j is the scale of wavelet decomposition, $d_j(k)$ is the coefficient of wavelet

244 decomposition, M and N are the length and width of images, ω is the wavelet
245 coefficient, λ is the set threshold, and $sign$ is the sign function. In this case, $M \times$
246 $N=2560 \times 1440$, $\alpha=0.5$.

247 **2.4 Correlation between color information and discharge**

248 The unstructured image data of mountain streams implicitly contains many stream
249 features relevant to discharge, such as the width and depth of streams, the coverage of
250 water surface, and spatial distributions of flow direction and flow velocity. CNN has
251 been widely used in various classification and regression problems for its capability in
252 recognizing the features of interest from images (Krizhevsky et al., 2017). In this study,
253 we attempted to achieve discharge monitoring by establishing empirical relationships
254 between the RGB color information of the water body and the discharge volumes. We
255 first explored the correlation between the combination of R/G/B values in the region of
256 interest (ROI, see Fig. 2) and the discharge conditions. Spearman's rank correlation
257 coefficient between RGB values and discharge is calculated as

$$258 \quad r_s = 1 - \frac{6 \sum_{i=1}^n d_i^2}{n(n^2-1)} \quad (5)$$

259 where n is the number of samples, d_i is the difference between the ranks of R/G/B values
260 and discharge of each image sample.

261

262 **2.5 Algorithms of discharge estimation**

263 We used three algorithms to establish discharge classification models (Fig. 2), including
264 convolutional neural network (CNN), support vector machine (SVM), and random

265 forest (RF). The data of the RGB color matrix derived from pre-processed images was
266 used as model inputs. SVM and RF were coupled with CNN to explore the potential
267 merits of traditional machine learning algorithms in improving the accuracy and
268 efficiency of CNN-based discharge classifiers. All the embedding image features are
269 normalized and regularized before passed to classifiers to avoid overfitting for CNN-
270 based models.

271 2.5.1 Convolutional Neural Network (CNN)

272 Deep convolutional neural network allows computational models composed of multiple
273 processing layers to learn representations of data with multiple levels of abstraction,
274 which have brought breakthroughs in processing images, video, speech, and audio
275 (Lecun et al., 2015). The AlexNet architecture (Krizhevsky et al., 2017) was used to
276 construct our model. Parameters of the semantic layer of the model were calibrated to
277 achieve feature extraction and classification of stream images. The image size was first
278 rescaled from 2560×1440 to 227×227 to facilitate the migration of trained AlexNet. A
279 227×227×3 (length×width×color) matrix was retrieved from each image as the model
280 input. There were five built-in convolutional layers, using a 3×3 convolution kernel and
281 a 3×3 pooled kernel. We replaced the last three layers of AlexNet with a full-connection
282 layer, a softmax layer, and a classification layer, leaving all other layers intact. The
283 parameters of the full-connection layer were set according to the number of selected
284 discharge values. The ReLU function was used as the convolutional layer activation
285 function to extract and pass on the water coverage features. The SoftMax function was

286 the activation function of the output layer, and the extracted feature vectors were
287 compressed under each discharge label. The probability that a stream image falls into a
288 discharge label was calculated as

$$289 \quad P(y|x) = \frac{e^{h(x,y_i)}}{\sum_{i=1}^n e^{h(x,y_i)}} \quad (6)$$

290 where x is the feature vector extracted by CNN, y is the discharge label, n is the number
291 of labels, $h(x, y_i)$ is the linear connectivity function. **The training method for CNN**
292 **was stochastic gradient descent with momentum, with 15 samples in small batches, a**
293 **maximum number of rounds of 10, a validation frequency of 3 epochs, and an initial**
294 **learning rate of 0.00005. The samples were shuffled in every epoch. The loss function**
295 **for discharge classification was Cross-Entropy Loss, as**

$$296 \quad L = -\frac{1}{N} \sum_{i=1}^N \sum_{c=1}^C y_{i,c} \log(p_{i,c}) \quad (7)$$

297 where L is the value of loss, N is the number of samples, C is the number of discharge
298 classes, $y_{i,c}$ represents the value of the true label for the i^{th} sample in the c^{th} class using
299 one-hot encoding, and $p_{i,c}$ represents the probability of i^{th} sample belonging to c^{th}
300 class calculated by CNN.

301

302 **2.5.2 Convolutional Neural Network coupled with Support Vector Machine** 303 **(CNN+SVM)**

304 SVM is a machine learning method based on structural risk minimization and Vapnik–
305 Chervonenkis (VC) dimension theory (Cortes and Vapnik, 1995). It has been widely
306 used in image processing, pattern recognition, fault diagnosis, prediction and

307 classification (Burges, 1998), which can help to capture key samples and eliminate
308 redundant samples by finding the optimal hyperplane. Compared with neural networks,
309 which rely on large training samples and tend to fall into local optima, SVM can achieve
310 global optima with a simpler model structure (Hanczar et al., 2010; Matykiewicz and
311 Pestian, 2012). However, the SVM-based classifier requires manual input of image
312 features. Therefore, we coupled CNN and SVM to achieve automatic discharge
313 classification. Image features extracted by CNN (i.e., the output of the 5th CNN pooling
314 layer) were fed into SVM classifiers to calculate discharge. **The extracted image
315 features were coded with "one-vs-all" scheme, and the linear kernel function was
316 selected for SVM classifier with hinge loss.**

317

318 **2.4.3 Convolutional Neural Network coupled with Random Forest (CNN+RF)**

319 RF (Tin Kam, 1995) is a flexible machine-learning algorithm that combines the output
320 of multiple decision trees to reach a single result. Each decision tree depends on the
321 values of a random vector sampled independently and with the same distribution for all
322 trees in the forest (Breiman, 2001; Panda et al., 2009). It is an integrated algorithm of
323 the Bagging type (Aslam et al., 2007) that combines multiple weaker classifiers, and
324 the final result is obtained by voting or averaging to improve accuracy and
325 generalization performance. We here used an RF with 350 decision trees and five
326 decision leaves. The coupling method of CNN+RF is similar to CNN+SVM, using the
327 same pooling outputs of CNN as the inputs of RF discharge classifiers.

328

329 **2.6 Model evaluation metrics**

330 The performance of discharge classification models was measured by four widely used
331 metrics, including classification accuracy, F1 score, coefficient of determination (R^2),
332 and root mean square error (RMSE).

333 (1) Accuracy:

$$334 \quad Accuracy = \frac{\sum_{i=1}^k TP_i}{N} \quad (8)$$

335 where TP_i is the number of correctly classified samples in the i^{th} discharge class; N is
336 the total number of samples; k is the number of discharge classes.

337 (2) F1 score:

$$338 \quad F1 = \frac{2 \times Precision \times Recall}{Precision + Recall} \quad (9)$$

339 where *Precision* is the ratio of true positive classification (TP_i) to the sum of TP_i and
340 the number of misclassified samples with the i^{th} discharge simulated by a model (FP_i);
341 *Recall* is the ratio of TP_i to the sum of TP_i and the number of misclassified samples
342 with the observed i^{th} discharge (FN_i), calculated as

$$343 \quad Precision = \sum_{i=1}^k \frac{n_i}{N} \times \frac{TP_i}{TP_i + FP_i} \quad (10)$$

$$344 \quad Recall = \sum_{i=1}^k \frac{n_i}{N} \times \frac{TP_i}{TP_i + FN_i} \quad (11)$$

345 where n_i is the number of samples that fall in the i^{th} class.

346 (3) R^2

$$347 \quad R^2 = 1 - \frac{\sum_{j=1}^N (y_j - \hat{y}_j)^2}{\sum_{j=1}^N (y_j - Y)^2} \quad (12)$$

348 where y_j and \hat{y}_j are the observed and simulated discharge, respectively; Y is the mean

349 discharge.

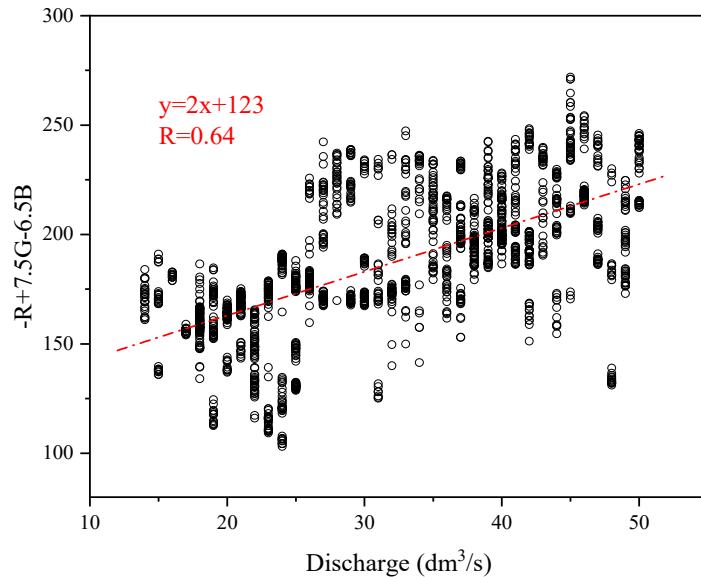
350 (4) RMSE

351
$$RMSE = \sqrt{\frac{1}{N} \sum_{j=1}^N (y_j - \hat{y}_j)^2} \quad (13)$$

352 3 Results

353 3.1 Correlation analysis

354 Traversing the common algebraic combinations of the three colors, we found that
355 $-\bar{R} + 7.5\bar{G} - 6.5\bar{B}$ (\bar{R} , \bar{G} , \bar{B} are the mean values of red, green and blue channels of
356 an image, respectively) had a spearman correlation coefficient of 0.67 with discharge
357 (p-value < 0.01), indicating that the discharge is significantly correlated with the color
358 combination value at the 99% confidence level (Fig. 5). Such result suggests that
359 discharge conditions are embedded in RGB information of mountain streams to some
360 extent, which could be further retrieved and refined by CNN models.



361

362 **Figure 5.** Correlation between RGB color values and corresponding discharges.

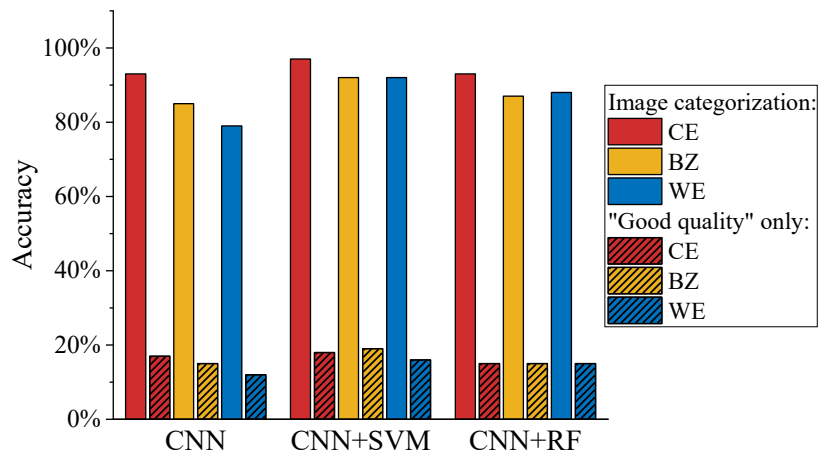
363

364 **3.2 Effectiveness of automated image categorization**

365 Most of the previous image-based studies only selected unblemished images for
366 discharge or velocity monitoring, which resulted in poor model performance under
367 environmental disturbances (Leduc et al., 2018; Chapman et al., 2020; Herzog et al.,
368 2022). In this study, we also included samples under the influence of vegetation
369 shadows and water reflection for model training. We selected approximately 100 stream
370 images corresponding to each discharge volume (at the interval of 0.001 m³/s) from the
371 pre-processed samples (3168 images in total). The databases of "Good quality",
372 "Middle shadow", "Below shadow", and "Water reflection" were approximately
373 sampled in the ratio of 7:0.6:1.4:1 (2146:244:437:341 images) to ensure the
374 representation of different environmental conditions. The samples were distributed
375 evenly in each discharge interval to avoid bias towards particular discharge conditions
376 and enhance model performance on high and low flows (Wang et al., 2023).

377 **Fig. 6** demonstrates the difference in accuracy of monitoring discharge by the
378 defective images, using two sets of models trained with only "Good quality" images
379 and samples filtered by automated image categorization, respectively. Results derived
380 from the three discharge classification models and three color-enhancing methods
381 consistently suggest that the procedure of automated image categorization can
382 significantly improve model performance in apprehending defective images.
383 Classification accuracy of the models trained with only "Good quality" samples
384 staggered between 11.8%-18.7%, while the accuracy of the models trained after

385 automated image categorization was higher than 79.0% (79.0%-97.4%) regardless of
 386 the choices of color processing method and deep learning model. The average
 387 difference in accuracy between the two sets of training samples reached 73.9%. The
 388 proportionate inclusion of defective images with vegetation shadow and water surface
 389 reflection enhances the anti-interference ability of the models in complex environments.
 390



391
 392 **Figure 6.** Accuracy of discharge classification of images under environmental
 393 disturbances. Bars with and without patterns show the results using the models trained
 394 with only "Good quality" samples and samples after automated image categorization,
 395 respectively. Color enhancement methods include Color Enhanced (CE), Binarization
 396 (BZ), and Water-color Enhanced (WE).

397

398 **3.3 Model training and validation**

399 After the treatments of color-enhancing, image denoising, and automated image
 400 categorization, the images were randomly divided into training and validation sets by
 401 the ratio of 7:3, and then used for model training and validation, respectively.

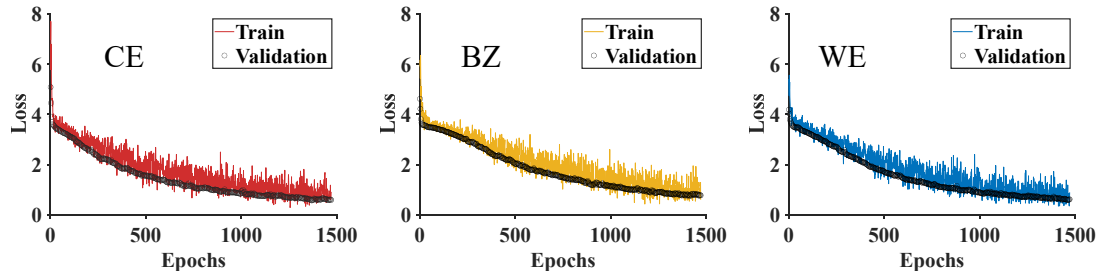
402

403 **3.3.1 Loss changes**

404 The changes in training and validation loss of the CNN models driven by three types of
405 color-enhanced images are demonstrated in **Fig. 7**. In the initial twenty epochs, the
406 training loss values decreased rapidly from 7.70 to 3.73 (Color Enhanced), from 5.91
407 to 3.73 (Binarization), and from 5.41 to 3.80 (Water-color Enhanced), respectively.
408 Subsequently, the decreasing rates slowed during the following 1000 epochs, averaging
409 around -0.0027 to -0.0030 per epoch. The loss value usually stabilizes after 1000 epochs
410 in CNN training (Keskar et al., 2016). In our case, the loss value began to flatten after
411 the 1300th epoch, signifying convergence towards a consistent loss value below 1.00
412 across all three color-enhancing methods. Therefore, we set the maximum training
413 epochs to 1470 to ensure model performance while avoiding overfitting.

414 The proximity between the training and validation loss changes at the final few
415 epochs is an important indicator that the model is not suffering from overfitting. A
416 commonly acknowledged benchmark of such proximity is approximately 0.1 to 0.2
417 (Heaton, 2018). In our CNN models, the validation loss values at the final epoch were
418 0.60, 0.78, and 0.63, respectively, which were 0.19, 0.08, and 0.07 lower than the
419 corresponding training loss. Such results suggest that the models did not suffer from
420 overfitting or underfitting.

421



422

423 **Figure 7.** Changes in training and validation loss of the models driven by three types
 424 of color-enhanced images. Color enhancement methods include Color Enhanced (CE),
 425 Binarization (BZ), and Water-color Enhanced (WE).

426

427 3.3.2 Comparison of discharge models

428 The heap map (**Fig. 8**) visualizes the performance of different models in classifying the
 429 validation image set with three tested color-enhancing methods under different
 430 environmental conditions. Results show that all three models (i.e., CNN, CNN+SVM,
 431 CNN+RF) can achieve satisfactory performance on discharge classification. The R^2
 432 under all environmental conditions was greater than 0.97, suggesting that the simulated
 433 discharge were significantly correlated to the flowmeters' measurement. The
 434 comparison of model performance generally shows consistency under different
 435 environmental conditions. Among the three models, CNN is more likely to over- or
 436 under-estimate discharge than both CNN+SVM and CNN+RF, with accuracy and F1
 437 score 8.6~13.4% and 0.084~0.115 lower than CNN+SVM and CNN+RF, respectively.
 438 CNN+RF achieved the best fit with the lowest RMSE. With all environmental
 439 conditions taken into account, CNN+SVM shows the best overall performance with the
 440 highest accuracy of 88.6%, the highest F1 score of 0.878, and the lowest RMSE of 1.08

441 dm^3/s . Such results could be related to the size of our samples and the characteristics of
442 the features extracted by deep layers of CNN. The features extracted from stream
443 images under one specific flow discharge show similarities, which highlights the
444 SVM's capability in classifying the embeddings from small samples with linear features.

445

446 **3.3.3 Comparison of color-enhancing methods**

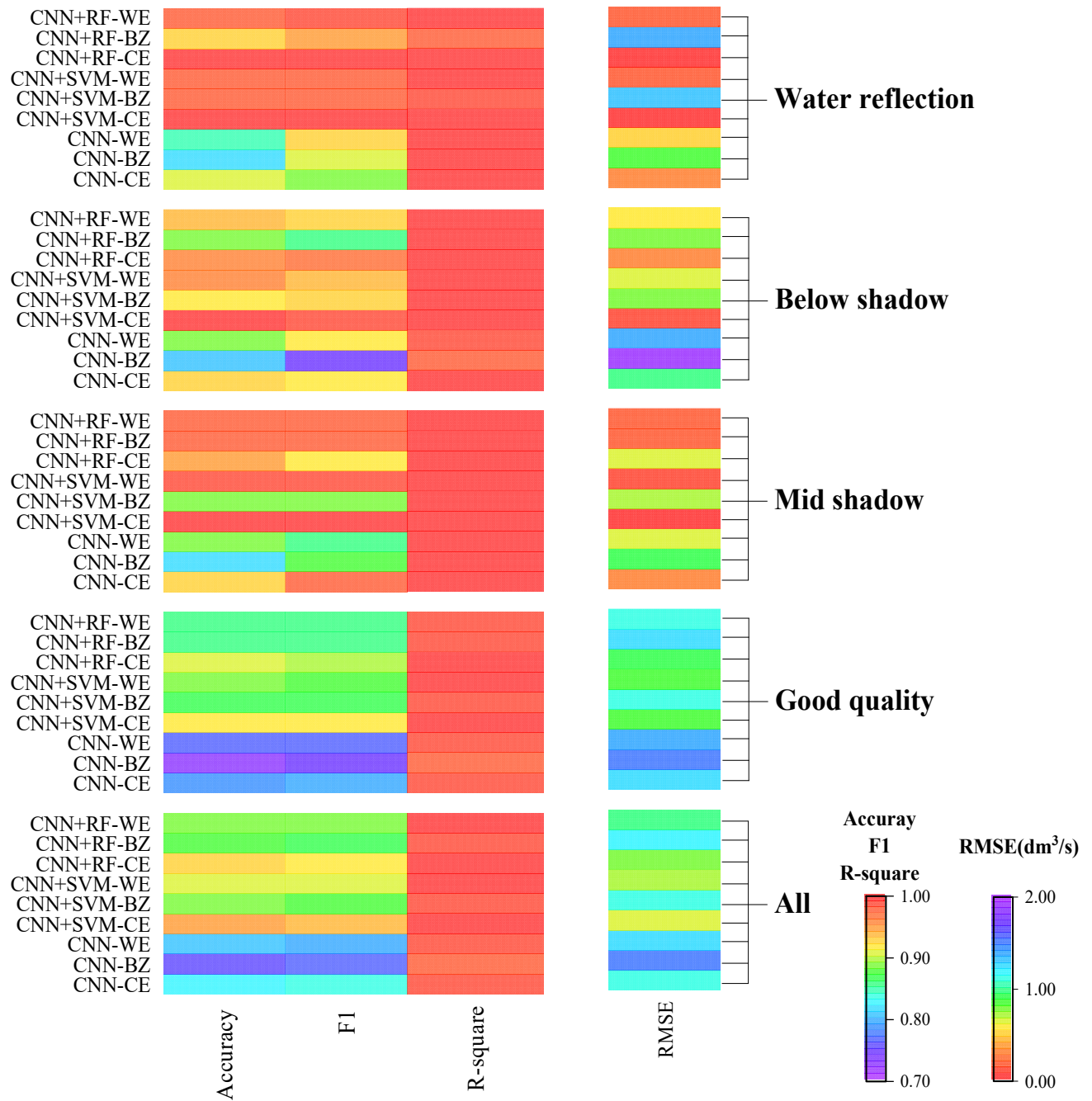
447 Among the three tested color-enhancing methods, the Color Enhanced approach
448 generally shows the best performance in discharge classification. Models driven by
449 Color Enhanced images achieved higher accuracy (+2.3%~+7.4%), higher F1 score
450 (+0.033~+0.067), and lower RMSE ($-0.068 \sim -0.415 \text{ dm}^3/\text{s}$) than those driven by
451 images processed with Binarization and Water-color Enhanced. This is partly due to the
452 different treatments in the edges of the water body. Binarization and Water-color
453 Enhanced relatively cause larger deviation from the real edges, while Color Enhanced
454 retains the image information to the maximum extent. Binarization reduces the cost of
455 computation and data storage by transforming raw stream images into binary images,
456 and thus facilitates real-time monitoring by embedded end-to-end devices (e.g., mobile
457 phones) with insufficient computing power (Shi et al., 2019). Considering that the color
458 and texture of the water surface vary significantly with discharge volumes while the
459 background is relatively stable, we proposed the Water-color Enhanced approach that
460 only processes color information within the water body. In our experiment, it took only
461 0.0154s to recognize flow discharge from one Binarization image with an Intel (R) Core

462 (TM) i7-10750H CPU, which was 36% and 22% faster than that of Color Enhanced
463 and Water-color Enhanced images, respectively. Such results suggest that it is
464 beneficial to retain the background information to the maximum extent and include the
465 non-water parts of mountain streams in image processing. However, future applications
466 of image-based discharge monitoring need to strike a balance between accuracy and
467 speed when choosing color processing methods.

468

469

470



471

472

473 **Figure 8.** Performance of discharge classification models under different

474 environmental conditions. Color enhancement methods include Color Enhanced (CE),

475 Binarization (BZ), and Water-color Enhanced (WE).

476

477 **4 Discussion**

478 The existing image-based methods usually rely on either the estimations of flow
479 velocity and cross-section area or assumptions on stage-discharge correlation (Tauro et
480 al., 2017; Leduc et al., 2018; Davids et al., 2019; Li et al., 2019). The first type of
481 method uses image-derived surface velocity to estimate sub-sectional mean streamflow
482 velocity and spatial integration of discharge (Le Coz et al., 2012). The difficulties in
483 capturing cross-sectional characteristics and the relationship between flow velocity and
484 water depth limit their application in small mountain streams. The second type of
485 method retrieves river geometry directly through remote sensing, yet the accuracy is
486 primarily determined by the empirical assumptions on the relationships among water
487 depth, velocity, and discharge (Gleason and Smith, 2014; Young et al., 2015). In this
488 study, we proposed a new camera-based method to directly establish the relationship
489 between the RGB matrixes of stream images and the classification probabilities of
490 discharge. The unique merit of the CNN-based model is its capability in automatically
491 extracting and refining discharge-related features from image samples, which improves
492 the accuracy and applicability of the model. Previous attempts suggest that the selection
493 of image features can significantly affect the performance on classification of stream
494 images (Tauro et al., 2014). For example, Chapman et al. (2020) manually extracted
495 features from pre- and post-weir images and used them as the inputs of machine

496 learning models. However, the dominant image features relating to stream discharge
497 could vary across different environments (e.g., topography, vegetation on river banks,
498 water quality), limiting the transferability of such manually identified features.

499 Weather conditions (e.g., sun position, fog, rain) are the most common difficulties
500 that reduce picture quality (Leduc et al., 2018). Therefore, we designed an automated
501 procedure for categorizing samples by their brightness and saturation: (a) select four
502 areas in the image as detection areas, (b) eliminate images with insufficient light or
503 raindrops on the lens, (c) identify thresholds and classify the remaining images into four
504 categories for further model training, including the images under the influence of
505 vegetation shadow and overexposure caused by water reflection in certain angles. Such
506 inclusion and categorization of defective samples have significantly enhanced the anti-
507 interference ability of the model, facilitating uninterrupted discharge monitoring
508 through the daytime. These factors and the thresholds of brightness and saturation are
509 site-specific and require manual trials to identify them. However, after adequate initial
510 calibration, an established model can be used for the same site for extended periods and
511 repeated installations of camera systems.

512 The training and validation of deep learning models require a large number of
513 representative samples (He et al., 2016). We collected a total of 7757 image samples
514 from July 20th to September 27th, 2022, and 3168 images were used for model training
515 and validation after image screening and categorization. Although we executed an
516 effective automatic categorization procedure on the acquired image samples, it is

517 undeniable that the training and validation sets didn't cover all environmental
518 disturbances. For example, the time of sunrise and sunset, the appearance of water
519 surface reflections, and the coverage of vegetation shadows are affected by the angles
520 of sunlight and vary with seasons. With sufficient artificial lighting or installation of a
521 night-vision infrared camera (Royem et al., 2012), the images during nighttime can also
522 be used for discharge monitoring after training. More image samples are needed to
523 enrich the representativeness of the model in further studies. Another limitation is that
524 we have focused on low and average flow conditions in the model training due to the
525 lack of high-quality flood samples. In tropical and subtropical mountain streams of
526 southern China, floods usually occur during rainstorms and only last for a short time.
527 Heavy rainfalls constantly block the camera lens with raindrops, and the rapid
528 streamflow movement during heavy rainfall tends to cause blurred images, which can
529 only be partly improved by increasing the shutter speed and adjusting the camera
530 position.

531

532 **5 Conclusions**

533 The results demonstrate the effectiveness of a novel method for discharge monitoring
534 of mountain streams using deep learning and a low-cost solar-powered commercial
535 camera (approximately \$200). The discharge-relevant stream features embedded in a
536 large number of RGB images can be implicitly recognized and retrieved by CNN to
537 achieve continuous discharge monitoring. Coupling CNN and traditional machine

538 learning methods can potentially improve model performance in discharge
539 classification to various extents. In this case, the accuracy of CNN+SVM and CNN+RF
540 were 9.1%~14.4% higher, while the F1 score were 0.084~0.115 higher compared to
541 CNN. Proper image pre-processing and categorization can largely enhance the
542 applicability of image-based discharge monitoring. In an environment under complex
543 disturbances such as mountain streams, image quality is constantly interfered with by
544 shadows of vegetation on the river banks. The automated image categorization
545 procedure can effectively recognize discharge from defective images by filtering
546 samples under different conditions and improve model robustness. The comparison of
547 the three color-enhancing approaches also confirms the importance of including the
548 non-water parts (e.g., large rocks) and retaining the background information to the
549 maximum extent in the image analysis.

550 The proposed method provides an inexpensive and flexible alternative apparatus for
551 continuous discharge monitoring at rocky upstream mountain streams, where it is
552 challenging to identify the cross-section shape or establish a stable stage-discharge
553 relationship. Site-specific field data is needed to identify the criteria for image
554 categorization and model validation. However, it circumvents the potential errors in
555 assuming cross-section characteristics, such as the relationship between water depth
556 and flow velocity, and represents a new direction for applying deep learning techniques
557 in acquiring high-frequency discharge data through image analysis.

558

559 **Code/Data availability**

560 The code and data are available upon request from the corresponding author.

561 **Author contribution**

562 KD and CF conceptualized the experiments. GY, ZZ, and QZ curated the data. All
563 authors participated in the investigation. CF, GY, ZZ, and QZ wrote the original draft
564 and visualized the data. KD reviewed and edited the final version of the manuscript.

565 **Competing interests**

566 The authors declare no competing interests.

567 **Acknowledgments**

568 This work was supported by the National Key Research and Development Program of
569 China (2021YFC3001000; 2021YFC3200205), the National Natural Science
570 Foundation of China (52379032; 51909285), the Guangdong Basic and Applied Basic
571 Research Foundation (2023A1515012241), and the Guangdong Provincial Department
572 of Science and Technology (2019ZT08G090).

573

574 **References**

575 Abdullah-Al-Wadud, M., Kabir, M. H., Dewan, M. A. A., and Chae, O.: A Dynamic
576 Histogram Equalization for Image Contrast Enhancement, IEEE Transactions on
577 Consumer Electronics, 53, 593-600, 10.1109/TCE.2007.381734, 2007.
578 Aslam, J. A., Popa, R. A., and Rivest, R. L.: On estimating the size and confidence of a

579 statistical audit, Proceedings of the USENIX Workshop on Accurate Electronic
580 Voting Technology, Boston, MA, 10.5555/1323111.1323119, 2007.

581 Breiman, L.: Random Forests, Machine Learning, 45, 5-32, 10.1023/A:1010933404324,
582 2001.

583 Burges, C. J. C.: A Tutorial on Support Vector Machines for Pattern Recognition, Data
584 Mining and Knowledge Discovery, 2, 121-167, 10.1023/A:1009715923555, 1998.

585 Canziani, A., Paszke, A., and Culurciello, E.: An Analysis of Deep Neural Network
586 Models for Practical Applications, ArXiv, abs/1605.07678, 7-14,
587 10.48550/arXiv.1605.07678, 2016.

588 Carlisle, D., Grantham, T. E., Eng, K., and Wolock, D. M.: Biological relevance of
589 streamflow metrics: Regional and national perspectives, Freshwater Science, 36,
590 927-940, 10.1086/694913, 2017.

591 Chang, F., Hong, W., Zhang, T., Jing, J., and Liu, X.: Research on Wavelet Denoising
592 for Pulse Signal Based on Improved Wavelet Thresholding, 2010 First International
593 Conference on Pervasive Computing, Signal Processing and Applications, Harbin,
594 China, 17-19 Sept. 2010, 564-567, 10.1109/PCSPA.2010.142, 2010.

595 Chapman, K. W., Gilmore, T. E., Chapman, C. D., Mehrubeoglu, M., and Mittelstet, A.
596 R.: Camera-based Water Stage and Discharge Prediction with Machine Learning,
597 Hydrol. Earth Syst. Sci. Discuss., 2020, 1-28, 10.5194/hess-2020-575, 2020.

598 Cheng, H. D. and Shi, X. J.: A simple and effective histogram equalization approach to
599 image enhancement, Digital Signal Processing, 14, 158-170,
600 10.1016/j.dsp.2003.07.002, 2004.

601 Clarke, R. T.: Uncertainty in the estimation of mean annual flood due to rating-curve
602 indefiniton, Journal of Hydrology, 222, 185-190, 10.1016/S0022-1694(99)00097-9,
603 1999.

604 Cortes, C. and Vapnik, V.: Support-vector networks, Machine Learning, 20, 273-297,
605 10.1007/bf00994018, 1995.

606 Council, N. R.: Assessing the national streamflow information program, National

607 Academies Press, 176 pp., 10.17226/10967, 2004.

608 Czuba, J. A., Foufoula-Georgiou, E., Gran, K. B., Belmont, P., and Wilcock, P. R.:
609 Interplay between spatially explicit sediment sourcing, hierarchical river-network
610 structure, and in-channel bed material sediment transport and storage dynamics,
611 Journal of Geophysical Research: Earth Surface, 122, 1090-1120,
612 10.1002/2016jf003965, 2017.

613 Davids, J. C., Rutten, M. M., Pandey, A., Devkota, N., van Oyen, W. D., Prajapati, R.,
614 and van de Giesen, N.: Citizen science flow – an assessment of simple streamflow
615 measurement methods, Hydrology and Earth System Sciences, 23, 1045-1065,
616 10.5194/hess-23-1045-2019, 2019.

617 Deweber, J. T., Tsang, Y. P., Krueger, D. M., Whittier, J. B., Wagner, T., Infante, D. M.,
618 and Whelan, G.: Importance of Understanding Landscape Biases in USGS Gage
619 Locations: Implications and Solutions for Managers, Fisheries, 39, 155-163,
620 10.1080/03632415.2014.891503, 2014.

621 Finlayson, G. D., Hordley, S. D., and Drew, M. S.: Removing Shadows from Images,
622 Computer Vision — ECCV 2002, Berlin, Heidelberg, 2002, 823-836, 10.1007/3-
623 540-47979-1_55, 2002.

624 Fujita, I., Muste, M., and Kruger, A.: Large-scale particle image velocimetry for flow
625 analysis in hydraulic engineering applications, Journal of Hydraulic Research, 36,
626 397-414, 10.1080/00221689809498626, 2010.

627 Fujita, I., Watanabe, H., and Tsubaki, R.: Development of a non-intrusive and efficient
628 flow monitoring technique: The space-time image velocimetry (STIV), International
629 Journal of River Basin Management, 5, 105-114, 10.1080/15715124.2007.9635310,
630 2007.

631 Gershon, R., Jepson, A. D., and Tsotsos, J. K.: Ambient illumination and the
632 determination of material changes, J Opt Soc Am A, 3, 1700-1707,
633 10.1364/josaa.3.001700, 1986.

634 Gleason, C. J. and Smith, L. C.: Toward global mapping of river discharge using

635 satellite images and at-many-stations hydraulic geometry, *Proceedings of the*
636 *National Academy of Sciences*, 111, 4788-4791, 10.1073/pnas.1317606111, 2014.

637 Hanczar, B., Hua, J., Sima, C., Weinstein, J., Bittner, M., and Dougherty, E. R.: Small-
638 sample precision of ROC-related estimates, *Bioinformatics*, 26, 822-830,
639 10.1093/bioinformatics/btq037, 2010.

640 Hannah, D. M., Demuth, S., van Lanen, H. A. J., Looser, U., Prudhomme, C., Rees, G.,
641 Stahl, K., and Tallaksen, L. M.: Large-scale river flow archives: importance, current
642 status and future needs, *Hydrological Processes*, 25, 1191-1200, 10.1002/hyp.7794,
643 2011.

644 He, K., Zhang, X., Ren, S., and Sun, J.: Deep residual learning for image recognition,
645 *Proceedings of the IEEE conference on computer vision and pattern recognition*, Las
646 Vegas, NV, USA, 770-778, 10.1109/cvpr.2016.90, 2016.

647 Heaton, J.: Ian Goodfellow, Yoshua Bengio, and Aaron Courville: *Deep learning: The*
648 *MIT Press, Genetic programming and evolvable machines*, 19, 305-307,
649 10.1007/s10710-017-9314-z, 2018.

650 Herzog, A., Stahl, K., Blauhut, V., and Weiler, M.: Measuring zero water level in stream
651 reaches: A comparison of an image-based versus a conventional method,
652 *Hydrological Processes*, 36, e14234, 10.1002/hyp.14658, 2022.

653 Jiang, P. T., Zhang, C. B., Hou, Q., Cheng, M. M., and Wei, Y.: LayerCAM: Exploring
654 Hierarchical Class Activation Maps for Localization, *IEEE Transactions on Image*
655 *Processing*, 30, 5875-5888, 10.1109/TIP.2021.3089943, 2021.

656 Karvonen, J.: Virtual radar ice buoys – a method for measuring fine-scale sea ice drift,
657 *The Cryosphere*, 10, 29-42, 10.5194/tc-10-29-2016, 2016.

658 Kasuga, K., Hachiya, H., and Kinoshita, T.: Quantitative Estimation of the Ultrasound
659 Transmission Characteristics for River Flow Measurement during a Flood, *Japanese*
660 *Journal of Applied Physics*, 42, 3212-3215, 10.1143/jjap.42.3212, 2003.

661 Keskar, N., Mudigere, D., Nocedal, J., Smelyanskiy, M., and Tang, P.: On Large-Batch
662 Training for Deep Learning: Generalization Gap and Sharp Minima, *arXiv preprint*

663 arXiv:1609.04836, 10.48550/arXiv.1609.04836, 2016.

664 Kim, W., Roh, S.-H., Moon, Y., and Jung, S.: Evaluation of Rededge-M Camera for
665 Water Color Observation after Image Preprocessing, *Journal of the Korean Society*
666 *of Surveying Geodesy Photogrammetry and Cartography*, 37, 167-175,
667 10.7848/ksgpc.2019.37.3.167, 2019.

668 Krizhevsky, A., Sutskever, I., and Hinton, G. E.: ImageNet classification with deep
669 convolutional neural networks, *Communications of the ACM*, 60, 84-90,
670 10.1145/3065386, 2017.

671 Le Coz, J., Camenen, B., Peyrard, X., and Dramais, G.: Uncertainty in open-channel
672 discharges measured with the velocity–area method, *Flow Measurement and*
673 *Instrumentation*, 26, 18-29, 10.1016/j.flowmeasinst.2012.05.001, 2012.

674 LeCun, Y., Bengio, Y., and Hinton, G.: Deep learning, *Nature*, 521, 436-444,
675 10.1038/nature14539, 2015.

676 Leduc, P., Ashmore, P., and Sjogren, D.: Technical note: Stage and water width
677 measurement of a mountain stream using a simple time-lapse camera, *Hydrology and*
678 *Earth System Sciences*, 22, 1-11, 10.5194/hess-22-1-2018, 2018.

679 Li, W., Liao, Q., and Ran, Q.: Stereo-imaging LSPIV (SI-LSPIV) for 3D water surface
680 reconstruction and discharge measurement in mountain river flows, *Journal of*
681 *Hydrology*, 578, 124099, 10.1016/j.jhydrol.2019.124099, 2019.

682 Matykiewicz, P. and Pestian, J.: Effect of small sample size on text categorization with
683 support vector machines, *Publication History*, 193-201 pp.,
684 10.5555/2391123.2391149, 2012.

685 McMillan, H., Freer, J., Pappenberger, F., Krueger, T., and Clark, M.: Impacts of
686 uncertain river flow data on rainfall-runoff model calibration and discharge
687 predictions, *Hydrological Processes: An International Journal*, 24, 1270-1284,
688 10.1002/hyp.7587, 2010.

689 Noto, S., Tauro, F., Petroselli, A., Apollonio, C., Botter, G., and Grimaldi, S.: Low-cost
690 stage-camera system for continuous water-level monitoring in ephemeral streams,

691 Hydrological Sciences Journal, 67, 1439-1448, 10.1080/02626667.2022.2079415,
692 2022.

693 Panda, B., Herbach, J., Basu, S., and Bayardo, R.: PLANET: Massively parallel
694 learning of tree ensembles with MapReduce, PVLDB, 2, 1426-1437,
695 10.14778/1687553.1687569, 2009.

696 Royem, A. A., Mui, C. K., Fuka, D. R., and Walter, M. T.: Technical Note: Proposing a
697 Low-Tech, Affordable, Accurate Stream Stage Monitoring System, Transactions of
698 the ASABE, 55, 2237-2242, 10.13031/2013.42512, 2012.

699 Sauvola, J. and Pietikäinen, M.: Adaptive document image binarization, Pattern
700 Recognition, 33, 225-236, 10.1016/s0031-3203(99)00055-2, 2000.

701 Shi, W., Jiang, F., Liu, S., and Zhao, D.: Image Compressed Sensing using
702 Convolutional Neural Network, IEEE Trans Image Process, 29, 375-388,
703 10.1109/TIP.2019.2928136, 2019.

704 Tauro, F., Grimaldi, S., and Porfiri, M.: Unraveling flow patterns through nonlinear
705 manifold learning, PLoS One, 9, e91131, 10.1371/journal.pone.0091131, 2014.

706 Tauro, F., Piscopia, R., and Grimaldi, S.: Streamflow Observations From Cameras:
707 Large-Scale Particle Image Velocimetry or Particle Tracking Velocimetry?, Water
708 Resources Research, 53, 10374-10394, 10.1002/2017wr020848, 2017.

709 Tauro, F., Tosi, F., Mattoccia, S., Toth, E., Piscopia, R., and Grimaldi, S.: Optical
710 Tracking Velocimetry (OTV): Leveraging Optical Flow and Trajectory-Based
711 Filtering for Surface Streamflow Observations, Remote Sensing, 10, 2010,
712 10.3390/rs10122010, 2018.

713 Tin Kam, H.: Random decision forests, Proceedings of 3rd International Conference on
714 Document Analysis and Recognition, Montreal, QC, Canada, 14-16 Aug. 1995, 278-
715 282 vol.271, 10.1109/ICDAR.1995.598994, 1995.

716 Tsubaki, R.: On the Texture Angle Detection Used in Space-Time Image Velocimetry
717 (STIV), Water Resources Research, 53, 10908-10914, 10.1002/2017wr021913, 2017.

718 Wang, R., Chaudhari, P., and Davatzikos, C.: Bias in machine learning models can be

719 significantly mitigated by careful training: Evidence from neuroimaging studies,
720 Proceedings of the National Academy of Sciences, 120, e2211613120,
721 10.1073/pnas.2211613120, 2023.

722 Yorke, T. H. and Oberg, K. A.: Measuring river velocity and discharge with acoustic
723 Doppler profilers, Flow Measurement and Instrumentation, 13, 191-195,
724 10.1016/s0955-5986(02)00051-1, 2002.

725 Young, D. S., Hart, J. K., and Martinez, K.: Image analysis techniques to estimate river
726 discharge using time-lapse cameras in remote locations, Computers & Geosciences,
727 76, 1-10, 10.1016/j.cageo.2014.11.008, 2015.

728 Zhang, D.: Fundamentals of Image Data Mining, Analysis, Features, Classification and
729 Retrieval, Springer, 7, 35-44, 10.1007/978-3-030-17989-2, 2019.

730